OHATERIALS CCHERCE

Contents lists available at ScienceDirect

Nano Materials Science

journal homepage: www.keaipublishing.com/cn/journals/nano-materials-science/



Investigation towards scalable processing of silicon/graphite nanocomposite anodes with good cycle stability and specific capacity



Maziar Ashuri ^{a,*}, Oianran He ^a, Yuzi Liu ^b, Leon L. Shaw ^a

- ^a Department of Mechanical, Materials and Aerospace Engineering, Illinois Institute of Technology, Chicago, IL, 60616, USA
- b Center for Nanoscale Materials (CNM), Argonne National Laboratory, Lemont, IL, 60439, USA

ARTICLE INFO

Keywords: Li-ion Battery Silicon Anode Polydopamine Nanocomposite Graphite Carbon Coating

ABSTRACT

Silicon/graphite (Si/Gr) nanocomposites with controlled void spaces and encapsulated by a carbon shell (Si/Gr@void@C) are synthesized by utilizing high-energy ball milling to reduce micron-sized particles to nanoscale, followed by carbonization of polydopamine (PODA) to form a carbon shell, and finally partial etching of the nanostructured Si core by NaOH solution at elevated temperatures. In particular, the effects of ball milling time and NaOH etching temperature on the electrochemical properties of Si/Gr@void@C are investigated. Increasing the ball milling time results in the improved specific capacity of Si-based anodes. Carbon coating further enhances the specific capacity and capacity retention over charge/discharge cycles. The best cycle stability is achieved after partial etching of the Si core inside Si/Gr@void@C particles at either 70 or 80 °C, leading to little or no capacity decay over 130 cycles. However, it is found that both carbon coating and NaOH etching processes cause some surface oxidation of the nanostructured Si particles derived from high-energy ball milling. The surface oxidation of the nanostructured Si results in decreases in specific capacity and should be minimized in future studies. The mechanistic understanding developed in this study paves the way to further improve the electrochemical performance of Si/Gr@void@C nanocomposites in future.

1. Introduction

Among the candidates for anode, silicon has gained a huge attention because it has more than 10 times of the theoretical specific capacity than graphite and it can be extracted easily from the earth crust. However, the anisotropic expansion and shrinkage of silicon (about 400%) during lithiation and delithiation, respectively, lead to cracking of silicon particles and repeated fracture and formation of solid electrolyte interphase (SEI) layers [1–4]. Pulverization of particles causes loss of the contact of Si particles with the conductive network, while repeated SEI formation deteriorates the electrolyte. All of these result in fast capacity decay and poor electrochemical performance [1–5].

Many attempts have been made in order to address the issues faced by Si anodes. Employing micron- and nano-sized silicon [6–8], trapping the silicon particles in conductive matrix [9,10], improving the binder and electrolytes [11–13], making porous Si structures [14–16], and yolk-shell design [17–20] are among those being attempted. Collectively, these extensive studies of Si anodes have revealed several important trends. First, reducing Si particle sizes to nanoscales can improve cycle stability because of the reduced tendency for particle cracking and smaller volume

In spite of significant potential for Si designs with a combination of nano-size, carbon coating and void space, many studies on yolk-shell design start with Si nanoparticles [17,21–23], which limits the potential of yolk-shell design for practical applications because of high costs of Si nanoparticles. In addition, yolk-shell design is often produced with the use of environmentally unfriendly HF solutions [17,21–23], which further limits its practical applications. Instead of starting with Si nanoparticles, many studies seek high-energy ball milling method to produce

E-mail address: mashuri@hawk.iit.edu (M. Ashuri).

https://doi.org/10.1016/j.nanoms.2019.11.004

change per particle during cycles [6–8]. Second, conductive coatings such as carbon can improve electronic conductivity on the surface of Si particles and increase the mechanical integrity [1,9]. Third, the void space inside the Si particle can provide space to accommodate volume expansion and shrinkage during charge/discharge cycles [17–20]. Fourth, a combination of nano-size, carbon coating and void space such as yolk-shell design and porous Si structures appears to offer the most promising long-cycle stability [14–19] because the void space accommodates the volume expansion, while the carbon shell confines the volume expansion inside the yolk-shell particle, improves electronic conductivity and provides a robust interface for a stable SEI layer and particle contact with the conductive additive and current collector.

^{*} Corresponding author.

low cost Si nano- or sub-micrometer particles [1,24–26]. In a recent study [26], we have combined high-energy ball milling with partial Si etching using a NaOH solution to create Si@void@C structure (similar to yolk-shell design) as the first attempt to produce Si anodes with a good combination of high performance and low cost. However, substantial improvement in the cycle stability of Si@void@C is still required to mature this technology.

Carbon coating is often pursued in making yolk-shell and Si@void@C designs [17,21–23,26]. There are multiple methods to form carbon coating such as chemical vapor deposition (CVD), thermal vapor deposition (TVD), hydrothermal, carbonization of carbon precursors, etc. [27–30]. Polydopamine (PODA) is considered as a powerful source of graphitized carbon. This biomolecule is shown to be capable of forming coatings on a wide range of substrates including polymers, ceramics and metals, and has the benefit of self-polymerization in basic solutions at room temperature which usually leads to high yield of carbon [31–36]. The polymerization is usually followed by a carbonization step at higher temperatures (typically 800 °C). The carbon layer can range from monolayer to multilayer [31–36]. Finally, it is worth to mention that the PODA coating can be utilized directly without the carbonization [37].

In this study, we have selected PODA as conductive carbon source to enhance the conductivity of the silicon/graphite (Si/Gr) composites. High-energy ball milling of a Si/Gr mixture is studied as a means to produce nanostructured Si/Gr particles from micrometer-sized Si and graphite powders. NaOH etching is investigated to create Si/Gr nanocomposites with engineered void space and encapsulated by a carbon shell, denoted as Si/Gr@void@C hereafter. Furthermore, the effects of key processing parameters, ball milling time and NaOH etching temperature, on the electrochemical properties of Si/Gr@void@C are investigated in detail to provide guidelines for future process optimization. To our knowledge, this is the first study on the effects of ball milling time and NaOH etching conditions, particularly their interplay, on the electrochemical properties of Si/Gr@void@C nanocomposites. The new insights established in this study can shed light on hidden aspects of the process and pave the way to large-scale production of the silicon-based nanocomposite anode material for Li-ion batteries in the future.

2. Experimental

2.1. Preparation of Si/Gr@void@C

Silicon powder (−325 mesh, 99% trace metals basis, Sigma Aldrich®) and TIMCAL TIMREX® BNB90 Expanded Graphite were utilized as starting materials without further purification. Silicon and graphite were mixed with the weight ratio of 9:1 and then loaded into the canister inside an Ar-filled glove box. The main purpose for adding 10 wt % graphite in the mixture was to mix the Si and graphite in nanoscale through high-energy ball milling so that all or most of the Si particles would be connected to the conductive network provided by graphite [26]. The ball to powder ratio was set to 10:1 to minimize the iron contamination. The mixture was ball milled for 2, 6 and 10 h using a SPEX mill to form ball milled Si/Gr powders. After each 30-min milling, the machine was stopped for 10 min to cool down and prevent too much cold welding of powder. After milling was finished, the canister was opened inside the glove box and the powder was collected. The procedure for the PODA coating started with dispersing the ball-milled powder in a Tris ($C_4H_{11}NO_3$) buffer solution (pH = 8.5 and 10 mM, BioWorld®) for 10 min, followed by addition of dopamine hydrochloride (C₈H₁₁NO₂·HCl, Sigma Aldrich®). The suspension was stirred overnight before centrifugation to collect the powder. The coated powder was washed with deionized water for 3 times and then dried at 80 $^{\circ}\text{C}$ for 12 h under vacuum. Carbonization of the PODA coating was performed inside a tube furnace under argon atmosphere by heating up to 400 $^{\circ}\text{C}$ for 2 h, followed by heating at 800 °C for 3 h to form the Si/Gr@C nanocomposite. Etching was then used to create void space in the Si/Gr@C nanocomposite to generate the Si/Gr@void@C powder. In the etching

process, the Si/Gr@C powder was dispersed in 0.5 M NaOH solution and stirred for 20 min. To amplify the etching process, the NaOH solution was preheated to 70 or 80 °C. The temperature was kept constant during the entire etching process. After 20 min etching, the solution was quickly centrifuged to prevent further etching. The solution was centrifuged, and then the collected powder was washed with DI water. The washing process was repeated three times. Finally, the powder was dried at 80 °C under vacuum overnight.

2.2. Cell construction

Electrochemical testing of the synthesized materials was done in $\ensuremath{\mathsf{CR2032}}$ coin cells through galvanostatic charge/discharge protocol. The working electrodes consisted of 60 wt % active material (Si/ Gr@void@C), 20 wt % polyacrylic acid (PAA, average molecular weight about 450,000 g mol⁻¹, Sigma Aldrich®) binder, and 20 wt % TIMCAL® conductive carbon black. The materials were mixed and hand ground in mortar and pestle. N-methyl-2-pyrrolidone (NMP, Sigma Aldrich®) was added to form a uniform slurry. The slurry was applied to a copper foil. The painted foil was vacuum-dried in an oven at 120 °C for 12 h. After drying, the foil was punched to make the working electrode. CR2032 coin cells were fabricated with lithium metal chips as both counter and reference electrodes. The electrolyte was 1 M lithium hexafluorophosphate (LiPF₆) salt dissolved in ethylene carbonate (EC)diethylene carbonate (DEC) with 1:1 vol ratio and 10 vol % fluoroethylene carbonate (FEC) as the additive to provide stable cycling. Celgard® 2325 film was used as the separator. Cycling and capacity retention were measured with Neware® battery test system at different current densities at room temperature. Specific capacities and current densities were normalized to the weight of the silicon content in the active material (BM Si/Gr@void@C). The average active material mass loading of the prepared electrodes was typically 1 mg cm⁻². Both cyclic voltammetry (CV) and electrochemical impedance spectroscopy (EIS) tests were performed employing Parstat 4000 (Princeton Applied Research®) in the same voltage window as cycling at a scan rate of 0.05 mV s⁻¹ and in the frequency range of 100 kHz to 1 Hz, respectively.

2.3. Structural and morphological characterization

The morphology, microstructure and elemental contents of powders were examined using JEOL JSM-5900LV scanning electron microscope (SEM) with accelerating voltage of 20 kV. SEM samples were first coated with gold using a sputter coater. Transmission electron microscopes (TEM) and energy-filtered TEM (EFTEM) in the Center for Nanoscale Materials (CNM) at Argonne National Laboratory (ANL) were employed to observe the carbon layer and internal voids along with the distribution of elements. X-ray diffraction (XRD) patterns were recorded using Bruker D2 Phaser with Bragg-Brentano geometry in the 2Θ range of 10° to 100° with Cu $K\alpha$ radiation (1.54056 Å). The powders were loaded in transparent quartz capillary tubes of 1.0 mm in diameter and wall thickness of 0.01 mm (purchased from Charles Supper Company) inside an Ar-filled glove box and mounted in a specially-fabricated PMMA holder with a groove to hold the capillary. Thermal gravimetric analysis (TGA) was measured using Mettler-Toledo® TGA-SDTA851e at a heating rate of 5 $^{\circ}\text{C}$ min⁻¹ under the flow of dry air, while the temperature range was 25-1000 °C. Specific surface areas (SSA) of various powders were measured using nitrogen adsorption experiments using Nova Quantachrome 2200e surface area & pore size analyzer. The SSA was calculated based on Brunauer-Emmett-Teller (BET) theory, while pore volume was obtained from Barrett-Joyner-Halenda (BJH) method. Raman spectroscopy was carried out using Renishaw® inVia confocal Raman microscope with laser excitation wavelength of 514 nm and the grating of 1800 lines mm^{-1} .

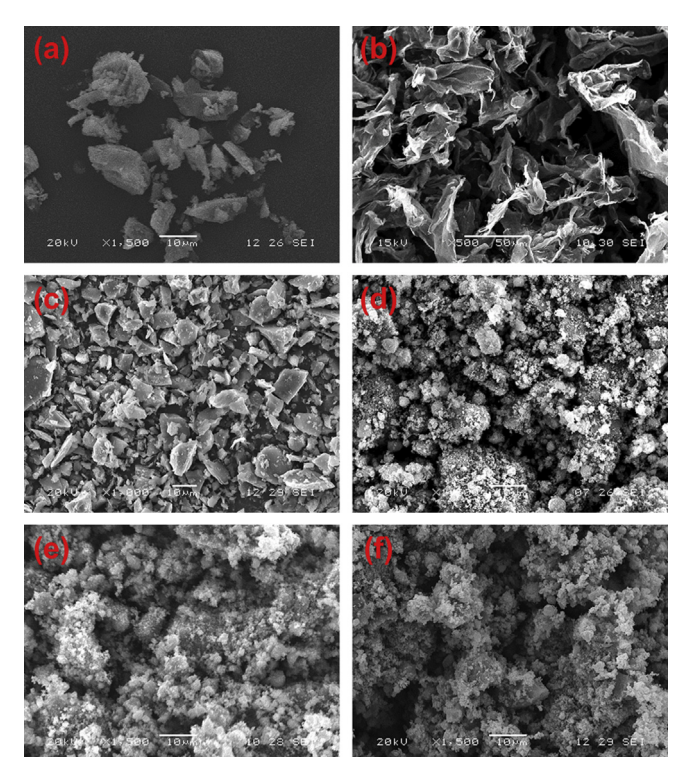


Fig. 1. SEM images: (a) silicon (Si) particles, (b) graphite (Gr) particles, (c) hand-mixed Si/Gr, (d) 2 h-BM Si/Gr, (e) 6 h-BM Si/Gr, and (f) 10 h-BM Si/Gr. The meaning of the sample ID can be found in Table 1.

3. Results and discussions

3.1. Powder characteristics of Si/Gr@void@C at different stages of synthesis

The as-received silicon and graphite particles are shown in Fig. 1(a)–(b), respectively. Silicon particles have irregular morphology with relatively large particle size (ranges from 5 to 40 µm) which is consistent with product details provided by the Sigma Aldrich® (~325 mesh). In contrast, graphite has flake-like morphology with 2D plate dimensions larger than 50 µm. As expected, hand mixing of silicon and graphite does not change the morphologies and particle sizes of both powders (Fig. 1c). However, ball milling has significantly reduced the particles sizes of both silicon and graphite powders and changed graphite from flake-like morphology to round particles, as revealed in Fig. 1(d)-1(f). The ball milled powders exhibit agglomeration with agglomerate sizes ranging from 1 µm to as large as 60 µm (see Figs. S1-S3 in Supplemental Material), while the primary particles forming these agglomerates have sizes in low sub-micrometer and nanometer ranges (see TEM and XRD analysis later). Increasing the ball milling time has made the sizes of primary particles more uniform and smaller.

To find out the degree of mixing of silicon and graphite as well as the possible contamination from the steel ball debris, several spots of ball milled powders were checked using the energy dispersive spectrometer (EDS) for each sample (Figs. S1–S3 and Tables S1–S3). Two trends are noted from the EDS analysis. First, the iron impurity from the steel balls increases with ball milling time and distributes everywhere in the 10-h ball milled sample (Table S3). However, the maximum iron impurity observed in the 10-h ball milled sample was no more than 3 wt % which is not expected to decrease the Si specific capacity much because Fe could react with Si to form FeSi/FeSi₂ in the subsequent high temperature reaction. Further, the elastic sites of a small amount of FeSi/FeSi₂

crystallites can act as buffers when Si expands during lithiation [38,39]. In addition, the Fe impurity will not increase the conductivity of the powder because of its small amount. Second, graphite has not been uniformly mixed with Si even after 10-h ball milling (Table S3). Since the detection volume for spot EDS analysis is about 1 μ m (in this study), this result indicates that at 1- μ m level many Si agglomerates do not contain graphite, and this is true for 2-h, 6-h and 10-h ball milled samples. It is anticipated that uniform mixing of Si and graphite can be enhanced if prolonged ball milling time is employed, but this will increase the Fe impurity level. Thus, we have limited ourselves to investigate the effects of 2- to 10-h ball milling times in this study. The result of many Si agglomerates with no graphite may suggest that there is no need to include graphite during ball milling, which should be investigated in the future.

To better understand the effects of ball milling time, specific surface areas (SSA) of powders with different ball milling times were measured through the BET method. As shown in Table 1, even 2-h ball milling has increased the SSA significantly (from 1.2 m² g⁻¹ for Si powder before ball milling to 10.2 m² g⁻¹ after 2-h ball milling). Furthermore, the SSA increases with ball milling time. Assuming that the ball milled particles have spherical shape and are composed of Si particles only, the equivalent particle size can be estimated. The estimated equivalent particle size exhibits a clear trend, that is, the equivalent particle size decreases with increasing ball milling time (Table 1). This trend is in excellent agreement with the SEM observations, i.e., primary particle sizes become more uniform and smaller as ball milling time increases (Fig. 1 and Fig. S1 -S3). It appears that the equivalent particle sizes of 6-h and 10-h ball milled powders (100 and 90 nm, respectively) are close to the sizes of primary particles forming agglomerates (to be discussed later with TEM images), suggesting that the ball milled (BM) Si/Gr agglomerates shown in Fig. 1 are loose agglomerates with open pores between primary particles. The pore volume has also increased drastically for all partially etched samples, as shown in Table 1. It is well known that the nitrogen adsorption method is only sensitive to pores with sizes <50 nm. Nevertheless, the consistent jump in the pore volume from $\sim 0.05 \text{ cm}^3 \text{ g}^{-1}$ for all of the un-etched samples to $\sim 0.3-0.4$ cm³ g⁻¹ for all of the etched

Table 1
Specific surface area, pore volume and equivalent particle size of Si/Gr@void@C nanocomposites at different stages of synthesis extracted from BET and BJH methods.

Processing Condition ^a	Specific Surface Area (m ² g ⁻¹)	Pore Volume (cm ³ g ⁻¹)	Equivalent Particle Size (nm)
Pure Silicon	1.227	0.003	1050
Pure Graphite	4.274	0.015	-
2 h-BM Si/Gr	10.219	0.042	130
2 h-BM Si/Gr@C	42.427	0.056	-
2 h-BM Si/ Gr@void@C-70	80.913	0.448	-
2 h-BM Si/ Gr@void@C-80	122.262	0.447	-
6 h-BM Si/Gr	12.408	0.045	100
6 h-BM Si/Gr@C	15.790	0.065	_
6 h-BM Si/ Gr@void@C-70	124.276	0.317	-
6 h-BM Si/ Gr@void@C-80	174.256	0.478	-
10 h-BM Si/Gr	14.003	0.058	90
10 h-BM Si/Gr@C	21.858	0.042	_
10 h-BM Si/ Gr@void@C-70	224.345	0.352	-
10 h-BM Si/ Gr@void@C-80	73.614	0.188	-

 $^{^{\}rm a}$ The meanings of sample IDs are as follows. 10 h-BM Si/Gr stands for 10 h ball milled Si/Gr mixture, while 10 h-BM Si/Gr@C represents 10 h-BM Si/Gr with carbon coating. 10 h-BM Si/Gr@void@C-70 and 10 h-BM Si/Gr@void@C-80 stand for 10 h-BM Si/Gr@C with NaOH etching at 70 $^{\circ}$ C and 80 $^{\circ}$ C, respectively. Other sample IDs with 2 h and 6 h refer to 2 h and 6 h ball milling, respectively, while keeping all other symbols with the same meanings as 10 h BM samples.

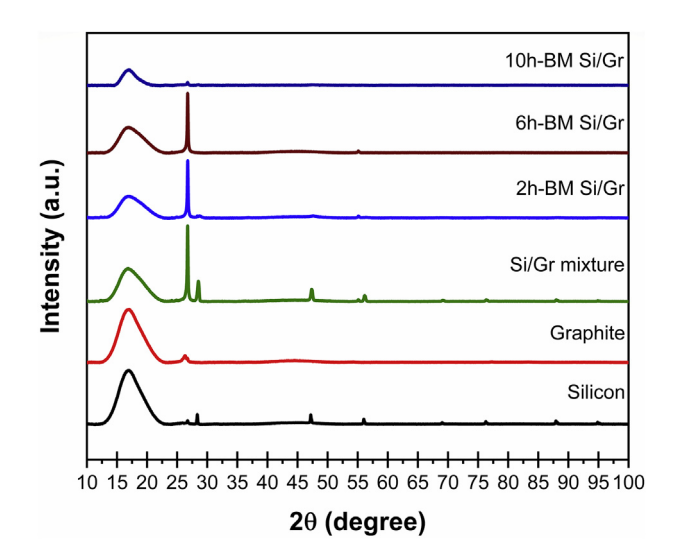


Fig. 2. XRD patterns of Si/Gr nanocomposites after different milling times as indicated. To better illustrate the effect of milling on the patterns, the XRD patterns of pure Si, pure graphite, and hand-mixed Si/Gr are provided. All patterns were collected in capillary tube.

samples reveals that partial etching of the Si core has taken place for all of the etched samples.

X-ray diffraction patterns of Si/Gr nanocomposites after 2, 6 and 10 h of ball milling are shown in Fig. 2. The patterns were collected in quartz capillary tubes and the sample loading was done inside the Ar-filled glovebox because the powders after ball milling became reactive and prone to oxidation. The XRD patterns of bare silicon and graphite powders were also collected in the capillary tube. These patterns helped us to check the presence of the crystalline phases during the synthesis. The silicon was detected with its characteristic peaks located at 28° , 47° , 56° and 69°. The graphite's major peak is located at 26.7°, but its intensity is very low even in the pure graphite case. This phenomenon can be attributed to the masking effect of the PMMA holder which has two strong peaks with one at 16° and the other at 26.7°. Since the amount of powder loaded in each tube was small and because of the masking effect of the PMMA holder, the data collection time was set as 10 h for each pattern to obtain a higher signal-to-noise ratio. Comparison between the patterns clearly shows the amorphization trend of powder. After 2- and 6h ball milling, the very low intensity peaks of silicon are still present. However, all Si peaks disappear after 10-h ball milling, suggesting that the sample has become amorphous. No pattern suggests the formation of any new compounds, such as silicon carbide, during high-energy ball milling. The particle size reduction and gradual amorphization of Si powders are in good accordance with the well-known phenomenon of repeated deformation, fracture, and cold welding of particles during high-energy ball milling, leading to the formation of nanostructured particles and eventual amorphization of particles [40–42].

TEM images and elemental mapping of Si/Gr nanocomposites ball milled for 2 h and coated with carbon (denoted as 2 h-BM Si/Gr@C hereafter) are shown in Fig. 3. The particles look dark under TEM with no signs of any voids inside. Elemental mapping reveals that the core of particles consists of silicon with some carbon. The latter is likely due to the TEM transmission mode of the carbon coating in imaging which overlaps with the nanostructured silicon core. The presence of the carbon coating is clearly visible and the thickness of the coating varies between 10 and 20 nm at different spots. This difference roots from the irregular morphology of the ball milled powder. Note that individual particle size is in the order of 100–200 nm even only after 2-h ball milling. These particle sizes are consistent with the equivalent particle size estimated from the SSA (Table 1), confirming that the agglomerates shown in Fig. 1d are loose agglomerates with average primary particle sizes near 130 nm.

The TEM images of the 2 h-BM Si/Gr@C nanocomposite after etching at 80 °C (denoted as 2 h-BM Si/Gr@void@C-80 hereafter) are very different from those before etching shown in Fig. 3. In particular, numerous voids are formed inside the particles, as evidenced by the numerous thickness contrast inside the particles (Fig. 4). These voids are distributed uniformly inside the particles and can accommodate the volume expansion of Si during its lithiation process in electrochemical testing. The elemental mapping shows uniform distribution of Si and C as well as the presence of a carbon coating. These findings are in good agreement with the data collected through the nitrogen adsorption test tabulated in Table 1. As mentioned before, high-energy ball milling has increased the SSA comparing to the starting silicon and graphite powders. The carbon coating derived from PODA further increases the SSA in all three ball milling conditions, indicating that the carbon coating is porous. This explains why partial etching of the nanostructured Si core can be done by the NaOH solution. After etching the SSA increases further, again for all three ball milling conditions (2, 6 and 10 h) and two etching temperatures (70 and 80 $^{\circ}$ C). The significant increase in the SSA after etching can be explained by partial etching of the Si core as revealed by TEM analysis.

Fig. 5 presents the XRD patterns of specimens before and after etching for all three ball milling conditions and two etching temperatures. The coating and coating process did not change the amorphous structure and no new crystalline phases were detected in the XRD patterns. No crystalline carbon peaks are observed either, suggesting that the carbon coating derived from PODA is amorphous. Additionally, the amorphous nature of Si/Gr@C was preserved for all three ball milling conditions after etching at both 70 and 80 $^{\circ}\text{C}.$

Fig. 6 illustrates the Raman spectra for the Si/Gr@C nanocomposite ball milled for 2 h before and after etching at 80 $^{\circ}$ C. The sharp peak

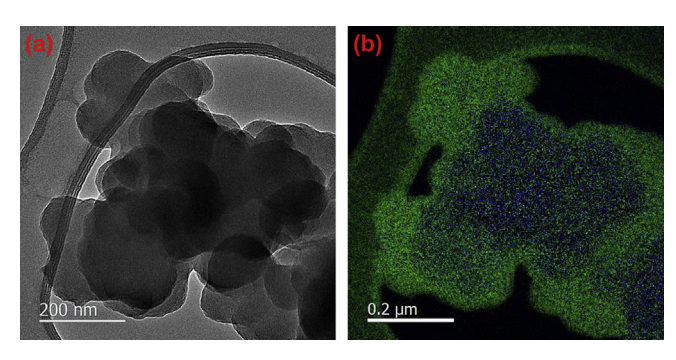


Fig. 3. (a) TEM image of 2 h-BM Si/Gr@C powder and (b) the corresponding elemental mapping of the powder in (a). Silicon element is represented with blue color, while carbon element is shown with green color.

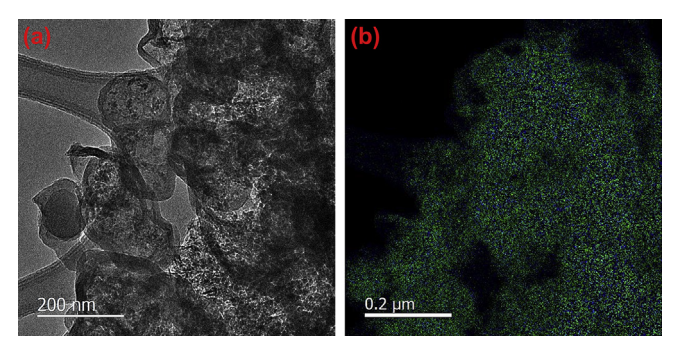


Fig. 4. (a) TEM image of 2 h-BM Si/Gr@void@C-80 powder and (b) the corresponding elemental mapping of the powder in (a). Silicon element is represented with blue color, while carbon element is shown with green color.

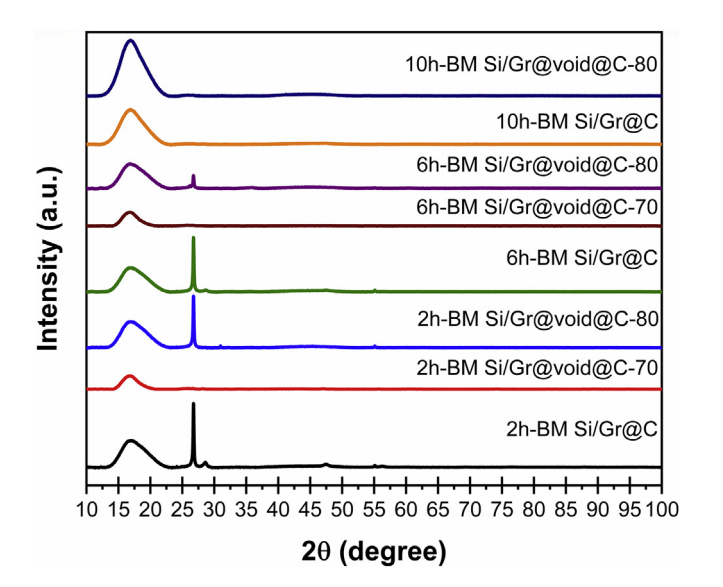


Fig. 5. XRD patterns of Si/Gr@void@C nanocomposites. The ball milling time and etching temperature for each sample are indicated in the figure. The broad peak at 17° and the sharp peak at 27° are both associated with the PMMA holder.

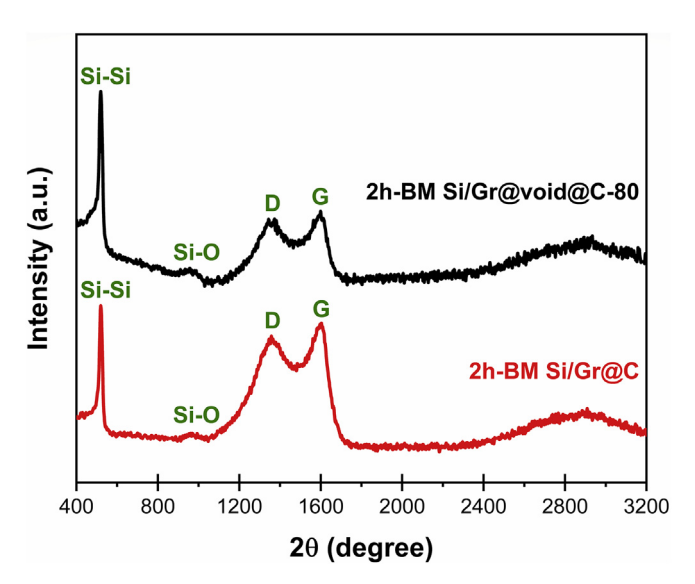


Fig. 6. Raman spectra of 2 h-BM Si/Gr@void@C-80 and 2 h-BM Si/Gr@C nanocomposites.

associated with 519 cm⁻¹ is related to crystalline silicon, while the broad peak positioned at 950 cm⁻¹ is assigned to Si–O formed on the surface of the material [43]. In both cases the silicon peak was observed which means that partial etching of the Si core has been achieved. The carbon coating derived from PODA results in the formation of both disorder-induced (D band) and graphitized (G band) carbon in Si/Gr@C and Si/Gr@void@C materials. The D band is associated with low symmetry carbon and defects in the structure, while G band originates from the stretch vibration of sp² hybrid orbital in the structure. The disordered carbon contains more defects with higher flexibility and less conductivity than graphitized carbon. However, the disordered carbon with more defects and vacancies has more sites for Li⁺ ions which improves the capacity of the battery [44-47]. The intensity ratio of the D band to G band (I_D/I_G) is 0.85 and 0.96 for the samples before and after etching, respectively. These ratios clearly illustrate the presence of significant disordered carbon in the samples, indicating that the carbonization condition (800 °C for 3 h) is not sufficient to fully graphitize the carbon.

To determine the carbon content in the final Si/Gr@void@C nano-composites for the three ball milling and two etching conditions, thermal gravimetric analysis (TGA) was performed under the flow of dry air for samples at various stages of synthesis (Fig. 7). Note that the TGA curves of Si/Gr@void@C nanocomposites are the combined effects of silicon weight gain and graphite weigh loss owing to oxidation of both Si and C, respectively, during heating in air. Therefore, to estimate the carbon content in Si/Gr@void@C nanocomposites, both of these processes should be considered. By considering how much carbon has been introduced in the carbon coating process and the final weight change of Si/Gr@void@C nanocomposites, one can estimate the carbon content in Si/Gr@void@C nanocomposites. The detailed procedure for this estimation is shown in Supplementary Material and the final results of the carbon content in each Si/Gr@void@C nanocomposite are summarized in Table 2.

3.2. Charge/discharge properties of Si/Gr@void@C nanocomposites

Fig. 8 consists of the cycle performance of Si/Gr@void@C nanocomposites at different stages of synthesis subjected to galvanostatic charge/discharge at different current rates. The data have been collected in CR2032 half-cell configuration with Li chip as both reference and counter electrode. The formation cycle protocol was 5 cycles at $0.05~A~g^{-1}$ followed by 5 cycles at $0.1~A~g^{-1}$ between 0.01~and~1~V. The voltage window for the rest of cycles was 0.1-1 V. The Si content in the active material (i.e., BM Si/Gr, BM Si/Gr@C, BM Si/Gr@void@C-70, and BM Si/Gr@void@C-80) is used to calculate the specific capacity data in the figure. The first cycle's voltage profiles of different samples are plotted and supplemented in Figs. S4-S6. In addition, the initial Coulombic efficiency of each battery is reported in Table S4. The effect of ball milling time is shown in Fig. 8a, while the effect of carbon coating can be derived from Fig. 8b. The effects of etching and etching temperature are shown in Fig. 8(c) and (d). It is very clear that the effects of these parameters on charge/discharge properties of Si-based electrodes are very complicated, but some important trends are present as discussed below.

First, as shown in Fig. 8a, the specific capacity of Si increases with ball milling time, i.e., 10 h-BM Si/Gr has the highest specific capacity, whereas 2 h-BM Si/Gr has the lowest one. This trend is related to the fact that longer ball milling time results in finer Si particles (Fig. 1 and Table 1). As particles become smaller, the specific surface area becomes larger and thus the interfacial area between Si particles and the liquid electrolyte becomes larger per unit Si mass. This increased interfacial area per unit Si mass results in faster lithiation/delithiation and thus larger specific capacity of Si for a given charge/discharge rate.

Second, the specific capacity of Si particles with 2 h ball milling becomes the largest after the carbon coating (Fig. 8b). That is, 2 h-BM Si/Gr@C has the highest specific capacity, whereas 10 h-BM Si/Gr@C has the lowest one. This new order of the specific capacity is completely opposite to that for the as-ball milled condition. In addition, it is noted that the specific capacities of 2 h-BM Si/Gr@C and 6 h-BM Si/Gr@C (Fig. 8b) are significantly higher than those of the corresponding ball-milled powders without the carbon coating (Fig. 8a). This significant enhancement is attributed to the carbon coating which improves the electronic conductivity on the surface of Si particles and thus accelerates the lithiation/delithiation process at the Si/electrolyte interface.

Third, in contrast to the significant specific capacity improvement displayed by 2 h- and 6 h-BM Si/Gr@C electrodes, 10 h-BM Si/Gr@C electrode actually exhibits a decrease in the specific capacity when compared with the counterpart without the carbon coating. This phenomenon occurs because of two competing processes taking place at the same time during the carbon coating process. One is the improvement in the electronic conductivity on the surface of Si particles induced by the carbon coating, as mentioned before. The other is the oxidation of Si surface by the water in the PODA aqueous solution to form SiOH which is dissociated to SiO⁻ and H⁺ in neutral and basic aqueous solutions [48].

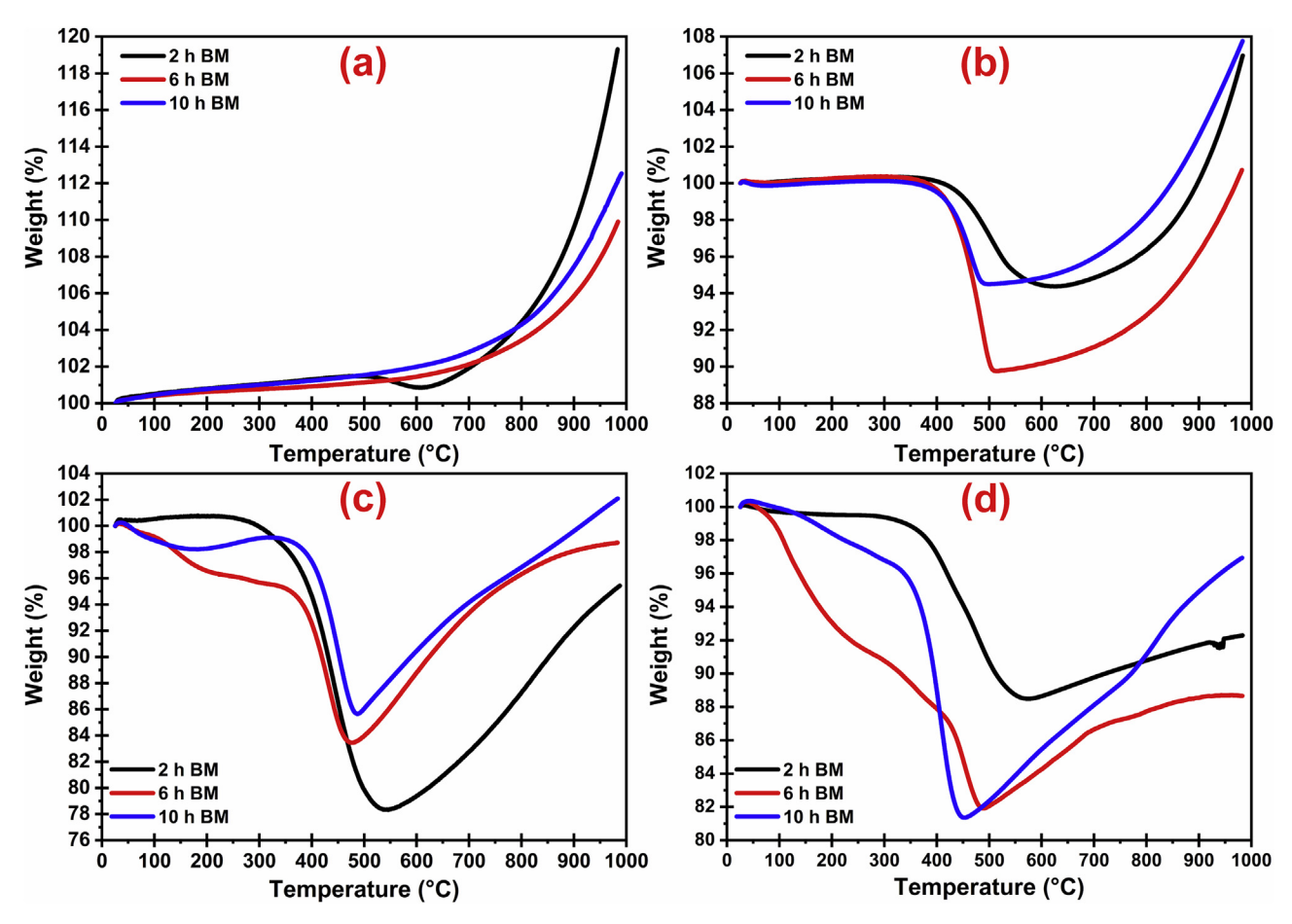


Fig. 7. TGA curves of Si/Gr@void@C nanocomposites at different stages of synthesis: (a) BM Si/Gr, (b) BM Si/Gr@C, (c) BM Si/Gr@void@C-70, and (d) BM Si/Gr@void@C-80. The ball milling time for each sample is indicated in the figure.

10 h-BM Si/Gr powder has a larger SSA than 2 h- and 6 h-BM Si/Gr powders (Table 1). Thus, more Si is oxidized during the carbon coating process for 10 h-BM Si/Gr powder than for the other two powders. The formation of SiO and SiOH reduces the quantity of Si available for lithiation/delithiation. This negative effect outweighs the positive effect of the carbon coating and thus decreases the specific capacity of 10 h-BM Si/Gr@C electrode. Note that the negative effect of forming SiO and SiOH on the surface of Si particles is also present for 2 h- and 6 h-BM Si/Gr powders, but they have smaller SSA than the 10 h-BM counterpart and thus less formation of SiO and SiOH. In fact, 2 h-BM Si/Gr powder has the smallest SSA among the three powders and thus the smallest formation of SiO and SiOH. As a result, its specific capacity exhibits the

Table 2Carbon content estimates for different Si/Gr@void@C nanocomposites with different processing conditions obtained from TGA curves.

Processing Condition	Carbon Content (wt. %)
Pure Silicon	0.0
Pure Graphite	100.0
2 h-BM Si/Gr	10.0
2 h-BM Si/Gr@C	19.6
2 h-BM Si/Gr@void@C-70	28.7
2 h-BM Si/Gr@void@C-80	31.0
6 h-BM Si/Gr	10.0
6 h-BM Si/Gr@C	17.4
6 h-BM Si/Gr@void@C-70	19.0
6 h-BM Si/Gr@void@C-80	27.2
10 h-BM Si/Gr	10.0
10 h-BM Si/Gr@C	13.7
10 h-BM Si/Gr@void@C-70	18.5
10 h-BM Si/Gr@void@C-80	22.5

largest improvement after the carbon coating (such as a drastic increase from 320 mA h $\rm g^{-1}$ to 1000 mA h $\rm g^{-1}$ at the 11th cycle at the current density of 0.2 A per gram of Si). 6 h-BM Si/Gr powder has the intermediate SSA and thus still experiences the positive effect of the carbon coating, showing the improvement in the specific capacity.

Fourth, all Si/Gr@void@C electrodes (Fig. 8c) exhibit significant decrease in the specific capacity when compared with the corresponding Si/Gr@C electrodes (Fig. 8b) before NaOH etching at 70 °C. This conspicuous trend is attributed to oxidation of the nanostructured Si core of the Si/Gr@C particles during etching, as explained below. The mechanisms to etch bulk Si wafers using NaOH and KOH solutions have been studied extensively [49–55]. It is generally agreed that hydroxide etching of Si is accompanied by a series of oxidation and reduction reactions which can be summarized in three steps: (1) silicate formation through silicon oxidation by hydroxyl groups, (2) water reduction and hydrogen release, and (3) evolution of complex compounds which are soluble in water. The reaction associated with each step is summarized below [49, 50].

(1) Oxidation of Si by hydroxyl radicals:

$$Si + 2OH^{-} \rightarrow Si(OH)_{2}^{2+} + 4e^{-}$$
 (1)

(2) Reduction of water:

$$2H_2O + 2e^- \rightarrow H_2 \uparrow + 2OH^-$$
 (2)

(3) Formation of a water-soluble complex:

$$Si(OH)_2^{2+} + 4e^- + 4H_2O \rightarrow Si(OH)_6^{2-} + 2H_2\uparrow$$
 (3)

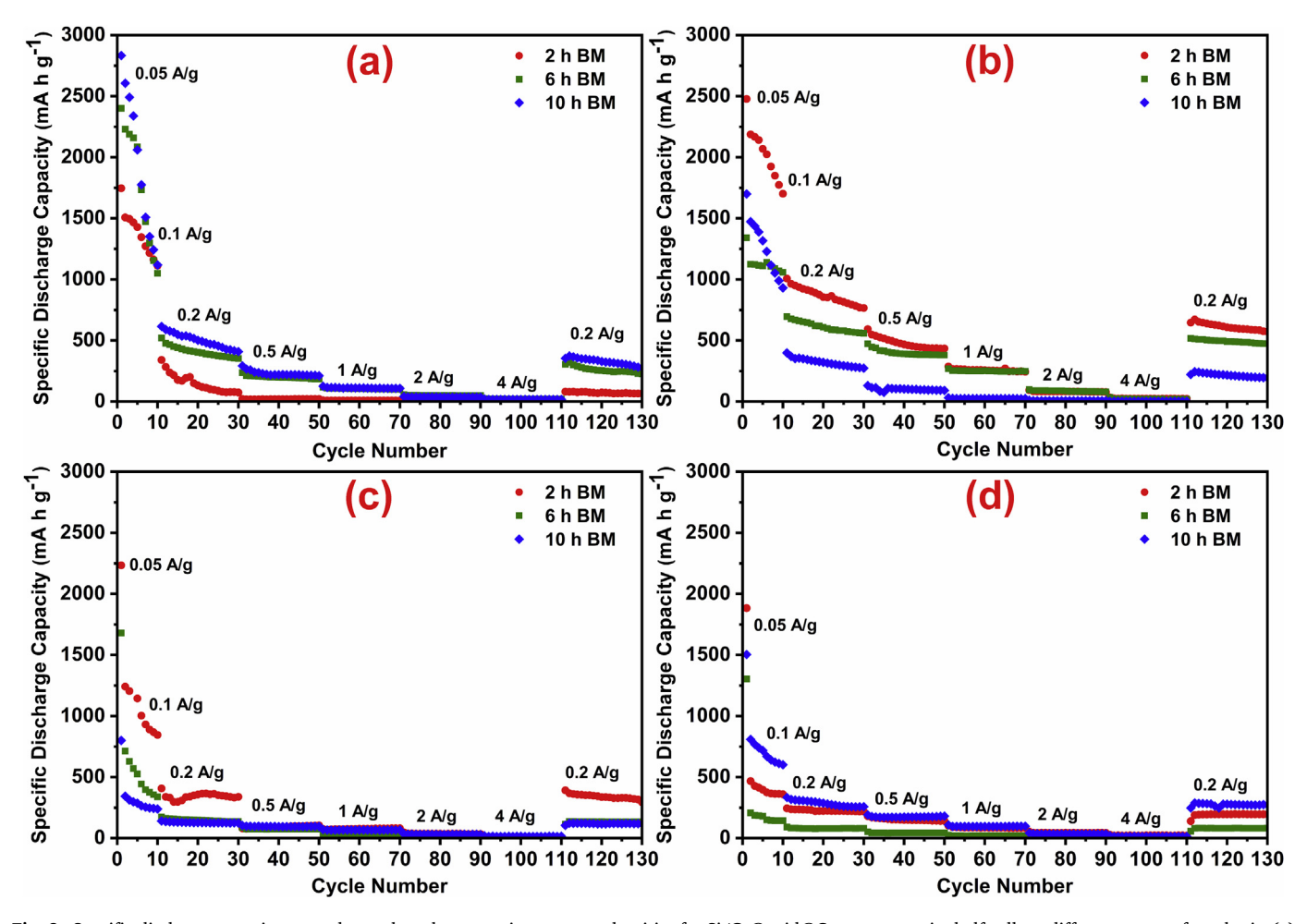


Fig. 8. Specific discharge capacity vs. cycle number plots at various current densities for Si/Gr@void@C nanocomposite half-cells at different stages of synthesis: (a) BM Si/Gr, (b) BM Si/Gr@C, (c) BM Si/Gr@void@C-70, and (d) BM Si/Gr@void@C-80. The ball milling time for each sample is indicated in the figure.

When it comes to etching of the nanostructured Si core of the Si/Gr@C particles, the same etching mechanism applies and results in the formation of Si/Gr@void@C particles with void space created inside Si/Gr@void@C particles as shown by TEM analysis (Fig. 4). However, nanostructured Si are chemically more active than bulk Si because of its high SSA. As a result, nanostructured Si is easily oxidized in aqueous solution even at room temperature [56,57]. For nanostructured Si, water could act as both acid and base, providing OH $^-$ and H $^+$ for oxidation of Si. Therefore, we hypothesize that the nanostructured Si core of the Si/Gr@C particles is partially oxidized during the NaOH etching process. Since the specific capacity of SiO $_{\rm x}$ (x \leq 2) is lower than that of Si [25], the specific capacities of all Si/Gr@C electrodes decrease after NaOH etching because of the partial replacement of the nanostructured Si by SiO $_{\rm x}$ (x \leq 2). This hypothesis is in good agreement with the cyclic voltammetry (CV) analysis (to be discussed later).

Fifth, NaOH etching at 80 °C results in even lower specific capacities (Fig. 8d) than etching at 70 °C (Fig. 8c) for both 2 h- and 6 h-BM powders. This trend suggests that there is more oxidation of the nanostructured Si core at 80 °C etching than at 70 °C etching. Experimentally, hydrogen bubbles were observed after about 5 min at 70 °C, whereas the bubbles appeared after only 2 min at 80 °C, indicating that etching kinetics has been enhanced at 80 °C but oxidation of the nanostructured Si core is accelerated as well (supported by the CV analysis below). Although both 2 h- and 6 h-BM powders etched at 80 °C have displayed lower specific capacities than their counterparts etched at 70 °C, 10 h-BM powder shows an opposite trend, i.e., the specific capacity of 10 h-BM Si/Gr@void@C etched at 80 °C is higher than that of the counterpart etched at 70 °C. This phenomenon is not fully understood yet but may be due to

its severe oxidation state before the etching starts. Additional studies on etching temperature effects are needed in the future to elucidate this phenomenon.

Sixth, although NaOH etching at both 70 $^{\circ}\text{C}$ and 80 $^{\circ}\text{C}$ has reduced the specific capacity of all Si/Gr@C powders, the resulting Si/ Gr@void@C powders after etching have exhibited much better cycle stability than the corresponding Si/Gr@C powders before etching. For example, 2 h-BM Si/Gr@C (Fig. 8b) lost about 25% capacity from the 10th cycle to 30th cycle at the current density of 0.2 A g^{-1} . In contrast, 2 h-BM Si/Gr@void@C-80 (Fig. 8d) displays only about 2% capacity decrease in the same cycle range at the same current density. Similarly, 6 h- and 10 h-BM Si/Gr@void@C powders have far better capacity retention than their Si/Gr@C counterparts. This salient trend is consistent with the concept that the voids inside Si/Gr@C particles can provide space to accommodate Si volume expansion during lithiation and thus little or no cracking of the carbon shell, thereby a stable electrode/ electrolyte interface, no repeated SEI layer fracture and formation, and thus stable cycle stability [14-20]. Therefore, it is important to conduct additional studies in the future to identify the optimized ball milling, carbon coating, and partial etching conditions so that oxidation of the nanostructured Si core can be minimized while sufficient partial etching of the nanostructured Si core can be achieved simultaneously.

3.3. Cyclic voltammetry and impedance analysis

To provide better understanding of the charge/discharge properties of Si/Gr@void@C at different stages of synthesis discussed above, CV experiments were conducted for all samples at different stages of

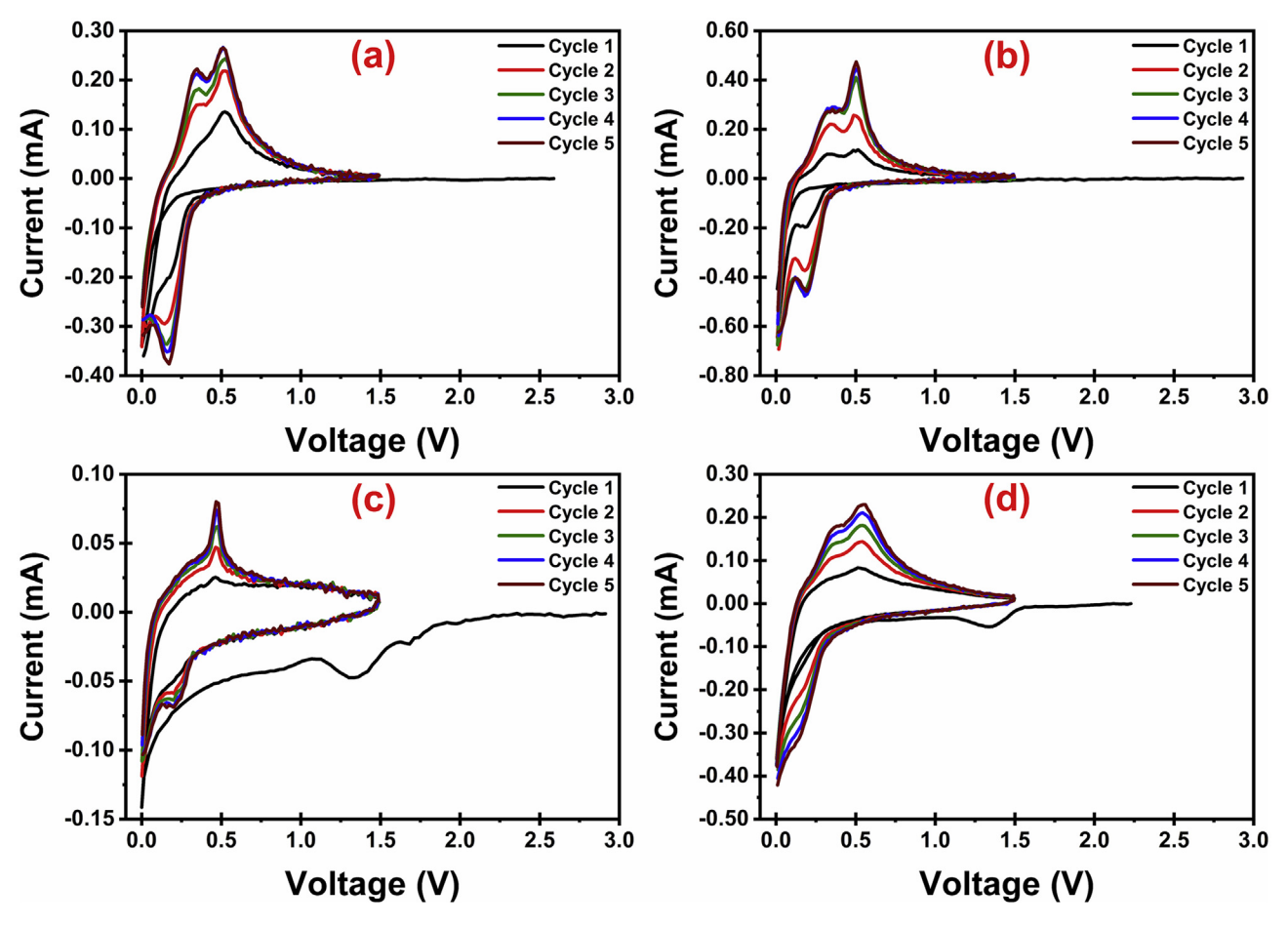


Fig. 9. Cyclic voltammogram (CV) curves of Si/Gr@void@C nanocomposite half-cells at different stages of synthesis: (a) 2 h-BM Si/Gr, (b) 2 h-BM Si/Gr@C, (c) 2 h-BM Si/Gr@void@C-70, and (d) 2 h-BM Si/Gr@void@C-80. The CV was conducted between 0.005 and 1.5 V at a scan rate of 0.05 mV s⁻¹ for 5 cycles.

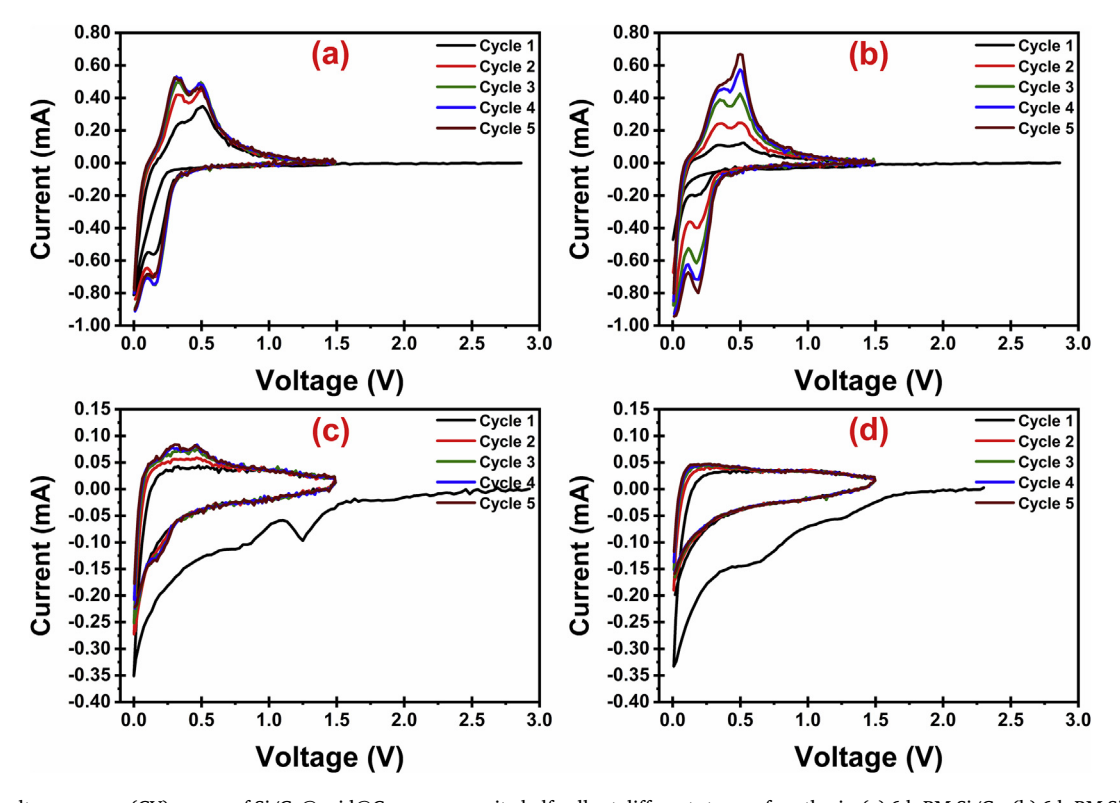


Fig. 10. Cyclic voltammogram (CV) curves of Si/Gr@void@C nanocomposite half-cells at different stages of synthesis: (a) 6 h-BM Si/Gr, (b) 6 h-BM Si/Gr@C, (c) 6 h-BM Si/Gr@void@C-70, and (d) 6 h-BM Si/Gr@void@C-80. The CV was conducted between 0.005 and 1.5 V at a scan rate of 0.05 mV s⁻¹ for 5 cycles.

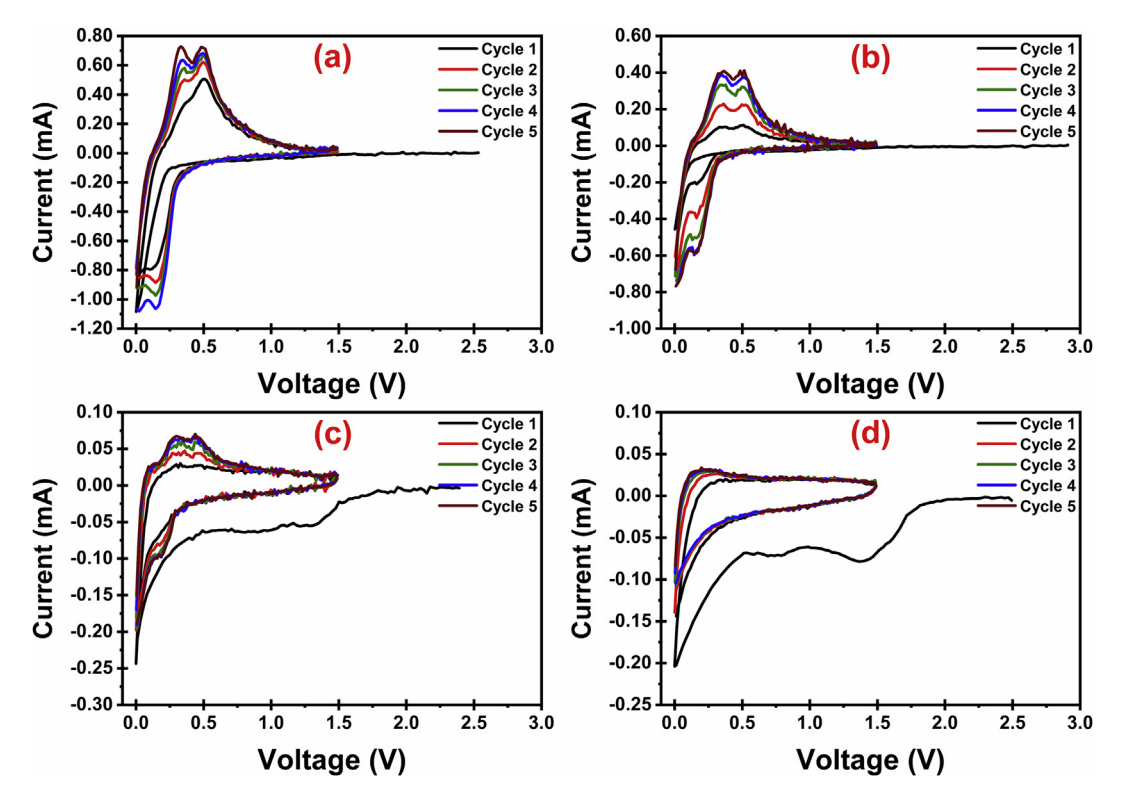


Fig. 11. Cyclic voltammogram (CV) curves of Si/Gr@void@C nanocomposite half-cells at different stages of synthesis: (a) 10 h-BM Si/Gr, (b) 10 h-BM Si/Gr@C, (c) 10 h-BM Si/Gr@void@C-70, and (d) 10 h-BM Si/Gr@void@C-80. The CV was conducted between 0.005 and 1.5 V at a scan rate of 0.05 mV s⁻¹ for 5 cycles.

synthesis. The CV results of 2 h-, 6 h- and 10 h-BM samples with and without carbon coating and etching are shown in Figs. 9–11, respectively. With the aid of these CV data the effects of ball milling, carbon coating, and etching on the charge/discharge properties of Si/Gr@void@C at different stages of synthesis can be better understood, as discussed below.

In all of the CV experiments, the first operation is the cathodic scan starting from the open circuit voltage (~3 V vs. Li/Li+) and ending at 0.005 V. As shown in Figure 9a, 2 h-BM Si/Gr electrode displays two strong cathodic peaks, one centered at $\sim 0.18 \text{ V}$ (vs. Li/Li⁺) and the other at the cut-off potential (0.005 V). The peak at \sim 0.18 V is related to the formation of metastable Li-Si amorphous phases (Li_xSi) [58,59], while the sharp peak at the cut-off potential is attributed to the phase transition of amorphous LixSi to crystalline Li15Si4 [60]. The anodic peaks are located at 0.38 and 0.56 V, corresponding to the step de-alloying from highly lithiated Si to less lithiated Si and finally to Si. The intensities of both cathodic and anodic peaks increase with cycle numbers because of the activation process of the electrode material, which is consistent with other similar studies [61-63]. The behavior of 2 h-BM Si/Gr@C electrode is similar to that of 2 h-BM Si/Gr but with stronger current, suggesting the improved lithiation/delithiation kinetics because of the presence of the carbon coating.

However, after partial etching of the nanostructured Si core by the NaOH solution at 70 and 80 °C, the CV curves of 2 h-BM Si/Gr@void@C electrodes (Fig. 9c and d) exhibit some features different from those of 2 h-BM Si/Gr and 2 h-BM Si/Gr@C (Fig. 9a and b). In particular, the cathodic peak at $\sim\!0.18$ V becomes very small for the 70 °C-etched electrode and almost disappears for the 80 °C-etched electrode. This trend unambiguously reveals less formation of amorphous Li_xSi phases for the etched samples than for the un-etched samples. One highly possible reason for this phenomenon to occur is the oxidation of the nanostructured Si core during etching, leading to less Si available to form amorphous Li_xSi phases during lithiation. This hypothesis is in good agreement with the CV curves of 6 h- and 10-h BM samples (to be discussed below). Another less obvious trend is the anodic peak at 0.38 V becomes weaker and broader after etching, indicating that the kinetics

for de-alloying from highly lithiated Si to less lithiated Si has become slower. This trend becomes stronger and obvious for 6 h- and 10 h-BM samples, probably induced by the presence of $SiO_x\ (x\leq 2)$ on the surface of the nanostructured Si core.

The third trend manifested by 2 h-BM samples is the appearance of the broad peak at 1.2-1.5 V for the sample etched at 70 °C (Fig. 9c) and the broad peaks at ~ 0.7 V and 1.2-1.5 V for the sample etched at 80 °C (Fig. 9d) in the first cathodic scan. The peak at ~ 0.7 V is known to correspond to the decomposition of EC/DEC and the peak at 1.2-1.5 V is related to the decomposition of FEC/VC to form SEI layer [64,65]. These peaks disappear in the subsequent cycles, indicating that most of SEI layer formation takes place in the first scan. Interestingly, these electrolyte decomposition peaks are not visible for the samples before etching (Fig. 9a and b). The possible reason for this discrepancy is that the etched samples have much larger SSA than the un-etched samples (Table 1). As a result, the etched samples have much more electrode/electrolyte interfacial area than the un-etched samples to induce the electrolyte decomposition and formation of SEI layer.

6 h- and 10 h-BM samples (Figs. 10 and 11) also possess the three trends discussed above for 2 h-BM samples but with the following two deviations. First, the cathodic peak at $\sim\!0.18$ V completely disappears in most cases (such as Fig. 10c, d, and 11d), suggesting the presence of substantial SiOx (x \leq 2) on the surface of the nanostructured Si core which reduces the kinetics to form amorphous LixSi phases as well as decreasing the quantity of Si available for lithiation. Second, the intensities of dealloying peaks at 0.38 and 0.56 V become weaker and broader, and these two peaks merge together for the samples etched at 80 °C, unequivocally showing that the kinetics for dealloying has reduced dramatically after etching, particularly after etching at 80 °C.

Note that all of the trends discussed above for the CV data can be rationalized as follows. The carbon coating has improved the lithiation and delithiation kinetics for both 2 h- and 6 h-BM samples, as evidenced by the increased currents of both cathodic and anodic peaks when compared with the counterparts without the carbon coating (Figs. 9 and 10). However, this is not the case for 10 h-BM sample (Fig. 11) because

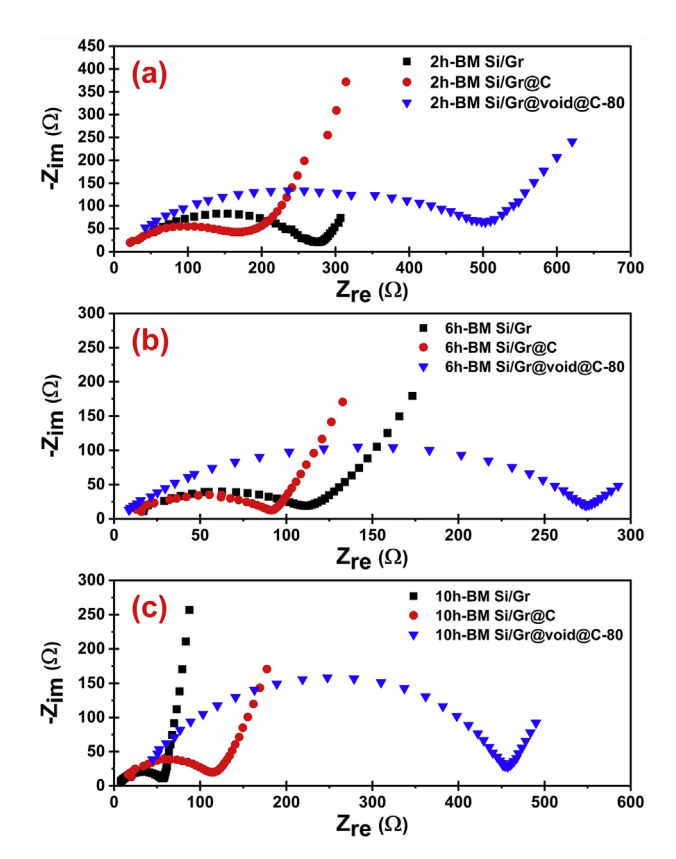


Fig. 12. Comparison between EIS spectra of Si/Gr@void@C nanocomposites after each step of synthesis, as indicated, for: (a) $2\ h$, (b) $6\ h$, and (c) $10\ h$ ball-milled powders.

the carbon coating process with aqueous PODA solution also introduces oxidation of the nanostructured Si core. 10 h-BM sample has a larger SSA than both 2 h- and 6 h-BM samples (Table 1) and thus is prone to oxidation which outweighs the benefit of the improved electronic conductivity provided by the carbon coating. Etching also results in some oxidation of the nanostructured Si core, leading to further reduction in the lithiation and delithiation kinetics as evidenced by the decreased currents of both cathodic and anodic peaks as well as merger of the dealloying peaks at 0.38 and 0.56 V. Etching at 80 °C causes more oxidation of the nanostructured Si core because the alloying peak at ~0.18 V has completely disappeared for both 6 h- and 10 h-BM samples (Figs. 10 and 11), while this peak has almost disappeared for 2 h-BM sample (Fig. 9). These trends are consistent with the trends with which the specific capacities of various samples change with the carbon coating, ball milling time, and etching temperature as shown in Fig. 8. Finally, it should be emphasized that although NaOH etching at 70 and 80 °C has caused some oxidation of the nanostructured Si core, partial etching of the nanostructured Si core has resulted in significant improvement in charge/discharge cycle stability (Fig. 8). Thus, the challenge is how to

Table 3
EIS data analysis using R(QR)W model.

Processing Condition	$R_{ohm}\left(\Omega\right)$	$R_{ct}\left(\Omega\right)$
2 h-BM Si/Gr	51.19	192.7
2 h-BM Si/Gr@C	22.92	106.7
2 h-BM Si/Gr@void@C-80	47.71	341.3
6 h-BM Si/Gr	14.04	74.46
6 h-BM Si/Gr@C	11.26	61.25
6 h-BM Si/Gr@void@C-80	10.56	228
10 h-BM Si/Gr	6.208	30.82
10 h-BM Si/Gr@C	15.23	75.34
10 h-BM Si/Gr@void@C-80	49.85	358.8

achieve cycle stability through partial etching while minimizing oxidation of the Si core and thus a limited decrease in the specific capacity. This topic deserves further investigation in the future.

To provide additional insights into the charge/discharge behavior of Si/Gr@void@C at different stages of synthesis, EIS analysis has been conducted. Nyquist plots of Si/Gr@void@C nanocomposites at different conditions are summarized in Fig. 12. The EIS measurements were performed after one day of fabrication of coin cells before the cycling process started. Nyquist plots of all cells have one depressed semicircle followed by a straight line at the low frequency region. It is known that the intercept of the semicircle with the real axis at the highest frequency, denoted as R_{ohm} in this study, reflects the sum of ohmic resistances of the electrolyte and the other resistive components such as separator, current collectors, and cell connectors [66]. The diameter of the depressed semi-circle is associated with charge transfer resistance (R_{ct}) , while the elongated tail indicates the diffusion of Li ions (Warburg impedance element) [67]. Recall that the EIS measurements were conducted before the charge/discharge cycles and thus all the cells have little or no SEI layers. Thus, the diameter of the depressed semi-circle does not contain the impedance from the SEI layer, R_{sei} . Using the equivalent circuit R(QR) W, the magnitude of R_{ohm} and R_{ct} have been quantified and listed in Table 3. A close examination of Table 3 reveals that both R_{ohm} and R_{ct} of 2 h- and 6 h-BM Si/Gr cells decrease after the carbon coating, unequivocally showing the benefit of improving the electronic conductivity on the surface of Si particles afforded by the carbon coating. This trend is in excellent agreement with the improved specific capacity of 2 h- and 6 h-BM Si/Gr@C cells shown in Fig. 8. In contrast to this trend, both Rohm and R_{ct} of 10 h-BM Si/Gr cells increase after the carbon coating, most likely resulting from the severe oxidation of the nanostructured Si core which outweighs the carbon coating benefit. This increase in R_{ohm} and R_{ct} is also reflected in the reduction of the specific capacity of 10 h-BM Si/Gr@C cells shown in Fig. 8.

Another salient trend exhibited by all cells is that R_{ohm} and R_{cb} particularly the latter, increase dramatically after NaOH etching of the nanostructured Si core at 80 °C, revealing that oxidation of the Si core during NaOH etching has led to harmful effect and increased the charge transfer impedance substantially. This harmful effect has manifested clearly in the decreased specific capacities of all Si/Gr@void@C-80 cells shown in Fig. 8. Table S5 contains a comparison between this work and other literature [29,68–71]. It highlights the advantage of engineered voids over other designs proposed for silicon anodes. However, it is necessary to minimize the partial oxidation of Si during etching. Thus, further investigation of NaOH etching conditions is required in the future to minimize oxidation of the nanostructured Si core while providing the engineered void space to improve cycle stability of Si anodes.

4. Conclusions

In summary, this study investigates a scalable, environmentally benign and potentially low cost process to fabricate silicon/graphite nanocomposites with engineered voids and encapsulated by a carbon shell (Si/Gr@void@C). This process starts with high-energy ball milling of micrometer-sized Si and graphite particles, followed by carbon coating with PODA precursor and finally partial Si etching with a NaOH solution at 70 or 80 °C. The effects of the ball milling time and NaOH etching temperature, particularly their interplay, on the electrochemical properties of Si/Gr@void@C are studied in detail. Through these investigations the following conclusions can be made.

(1) High-energy ball milling improves the specific capacity of Si anode because of the reduction of primary particle sizes from micrometers to around 100 nm. 10-h ball milling is more effective in enhancing the specific capacity than 2-h ball milling because the former leads to finer particle sizes and larger specific surface area than the latter. However, all ball-milled samples exhibit rapid capacity decay in the first 30 cycles.

- (2) 10-h ball milling is not sufficient to mix Si and graphite uniformly at the sub-micrometer scale. As a result, many ball-milled particles are composed of Si only. This result may suggest that there is no need for adding some graphite in the ball milling process, which should be investigated in the future.
- (3) The PODA-derived carbon coating improves the cycle stability as well as the specific capacity of Si/Gr@C anode because of the improved electronic conductivity and mechanical integrity derived from the carbon coating. The carbon coating process using PODA as the precursor also causes surface oxidation of ball-milled Si particles. 2 H ball-milled sample displays the largest improvement in the specific capacity because it has limited specific surface area and thus the benefit of the improved electronic conductivity outweighs the shortcoming of surface oxidation of ball-milled Si particles. 10-h ball-milled sample exhibits a slight decrease in the specific capacity because the drawback of surface oxidation outweighs the benefit of the improved electronic conductivity.
- (4) The engineered voids generated through partial etching of the nanostructured Si core inside the carbon shell using a NaOH solution at 70 and 80 °C have improved the cycle stability of Si/ Gr@void@C anode, but also resulted in lower specific capacity. The NaOH etching provides engineered voids to accommodate silicon expansion and shrinkage during lithiation/delithiation, but also leads to surface oxidation of the nanostructured Si core. As a result, the cycle stability is improved, but the specific capacity is reduced.
- (5) In general, etching at 80 °C results in more surface oxidation of the nanostructured Si core than etching at 70 °C. However, the effects of etching on the electrochemical properties also depend on the ball milling time. At 70 °C etching condition, 2-h ball-milled sample exhibits a good combination of superior discharge capacity and stable capacity retention. At 80 °C etching condition, 10-h ball-milled sample has high specific capacity than 2-h and 6-h ball-milled samples. The complicated interplay between the ball milling time and NaOH etching temperature needs to be further investigated in the future to develop better mechanistic understanding and optimized processing conditions for Si/Gr@void@C anodes with high specific capacity and good cycle stability.

Declaration of competing interest

No conflicting interest is declared.

Acknowledgements

MA and LS are grateful to the Rowe Family Endowment Fund, and QH acknowledges Tang Fellowship. The financial support from the U.S. National Science Foundation (NSF) with the award number CMMI-1660572 is acknowledged. Further, the discussion of TEM images with Dr. Satyanarayana Emani is appreciated. The use of the Center for Nanoscale Materials, an Office of Science user facility, was supported by the U.S. Department of Energy, Office of Science, Office of Basic Energy Sciences, under Contract No. DE-AC02-06CH11357.

Appendix A. Supplementary data

Supplementary data to this article can be found online at https://doi.org/10.1016/j.nanoms.2019.11.004.

References

- M. Ashuri, Q. He, L.L. Shaw, Silicon as a potential anode material for Li-ion batteries: where size, geometry and structure matter, Nanoscale 8 (2016) 74–103.
- [2] M.N. Obrovac, V.L. Chevrier, Alloy negative electrodes for Li-ion batteries, Chem. Rev. 114 (2014) 11444–11502.
- [3] X. Zuo, J. Zhu, P. Müller-Buschbaum, Y.-J. Cheng, Silicon based lithium-ion battery anodes: a chronicle perspective review, Nano Energy 31 (2017) 113–143.

- [4] C.K. Chan, H. Peng, G. Liu, K. McIlwrath, X.F. Zhang, R.A. Huggins, Y. Cui, High-performance lithium battery anodes using silicon nanowires, Nat. Nanotechnol. 3 (2008) 31–35.
- [5] Y. Sun, N. Liu, Y. Cui, Promises and challenges of nanomaterials for lithium-based rechargeable batteries, Nat. Energy 1 (2016), 16071.
- [6] U. Kasavajjula, C. Wang, A.J. Appleby, Nano- and bulk-silicon-based insertion anodes for lithium-ion secondary cells, J. Power Sources 163 (2007) 1003–1039.
- [7] R. Teki, M.K. Datta, R. Krishnan, T.C. Parker, T.-M. Lu, P.N. Kumta, N. Koratkar, Nanostructured silicon anodes for lithium ion rechargeable batteries, Small 5 (2009) 2236–2242.
- [8] H. Wu, Y. Cui, Designing nanostructured Si anodes for high energy lithium ion batteries, Nano Today 7 (2012) 414–429.
- [9] M.L. Terranova, S. Orlanducci, E. Tamburri, V. Guglielmotti, M. Rossi, Si/C hybrid nanostructures for Li-ion anodes: an overview, J. Power Sources 246 (2014) 167–177.
- [10] J. Luo, B. Ma, J. Peng, Z. Wu, Z. Luo, X. Wang, Modified chestnut-like structure silicon carbon composite as anode material for lithium-ion batteries, ACS Sustain. Chem. Eng. 7 (2019) 10415–10424.
- [11] S.S. Zhang, A review on electrolyte additives for lithium-ion batteries, J. Power Sources 162 (2006) 1379–1394.
- [12] D. Mazouzi, Z. Karkar, C. Reale Hernandez, P. Jimenez Manero, D. Guyomard, L. Roué, B. Lestriez, Critical roles of binders and formulation at multiscales of silicon-based composite electrodes, J. Power Sources 280 (2015) 533–549.
- [13] A. Mery, P. Bernard, A. Valero, J.P. Alper, N. Herlin-Boime, C. Haon, F. Duclairoir, S. Sadki, A polyisoindigo derivative as novel n-type conductive binder inside Si@C nanoparticle electrodes for Li-ion battery applications, J. Power Sources 420 (2019) 9–14.
- [14] J. Cho, Porous Si anode materials for lithium rechargeable batteries, J. Mater. Chem. 20 (2010) 4009–4014.
- [15] R. Yi, F. Dai, M.L. Gordin, S. Chen, D. Wang, Micro-sized Si-C composite with interconnected nanoscale building blocks as high-performance anodes for practical application in lithium-ion batteries, Adv. Energy Mater. 3 (2013) 295–300.
- [16] H. Tian, X. Tan, F. Xin, C. Wang, W. Han, Micro-sized nano-porous Si/C anodes for lithium ion batteries, Nano Energy 11 (2015) 490–499.
- [17] N. Liu, H. Wu, M.T. McDowell, Y. Yao, C. Wang, Y. Cui, A yolk-shell design for stabilized and scalable Li-ion battery alloy anodes, Nano Lett. 12 (2012) 3315–3321.
- [18] L.Y. Yang, H.Z. Li, J. Liu, Z.Q. Sun, S.S. Tang, M. Lei, Dual yolk-shell structure of carbon and silica-coated silicon for high-performance lithium-ion batteries, Sci. Rep. 5 (2015), 10908.
- [19] M. Ashuri, Q. He, Y. Liu, K. Zhang, S. Emani, M.S. Sawicki, J.S. Shamie, L.L. Shaw, Hollow silicon nanospheres encapsulated with a thin carbon shell: an electrochemical study, Electrochim. Acta 215 (2016) 126–141.
- [20] M. Ashuri, Q. He, K. Zhang, S. Emani, L.L. Shaw, Synthesis of hollow silicon nanospheres encapsulated with a carbon shell through sol–gel coating of polystyrene nanoparticles, J. Sol. Gel Sci. Technol. 82 (2017) 201–213.
- [21] S. Chen, M.L. Gordin, R. Yi, G. Howlett, H. Sohn, D. Wang, Silicon core-hollow carbon shell nanocomposites with tunable buffer voids for high capacity anodes of lithium-ion batteries, Phys. Chem. Chem. Phys. 14 (2012) 12741–12745.
- [22] J. Xie, L. Tong, L. Su, Y. Xu, L. Wang, Y. Wang, Core-shell yolk-shell Si@C@Void@C nanohybrids as advanced lithium ion battery anodes with good electronic conductivity and corrosion resistance, J. Power Sources 342 (2017) 529–536.
- [23] Y. Park, N.-S. Choi, S. Park, S.H. Woo, S. Sim, B.Y. Jang, S.M. Oh, S. Park, J. Cho, K.T. Lee, Si-encapsulating hollow carbon electrodes via electroless etching for lithium-ion batteries, Adv. Energy Mater. 3 (2013) 206–212.
- [24] M. Yoshio, T. Tsumura, N. Dimov, Electrochemical behaviors of silicon based anode material, J. Power Sources 146 (2005) 10–14.
- [25] M. Jana, R.N. Singh, A facile route for processing of silicon-based anode with high capacity and performance, Materialia 6 (2019) 100314.
- [26] M. Ashuri, Q. He, Y. Liu, S. Emani, L.L. Shaw, Synthesis and performance of nanostructured silicon/graphite composites with a thin carbon shell and engineered voids, Electrochim. Acta 258 (2017) 274–283.
- [27] M. Yoshio, H. Wang, K. Fukuda, T. Umeno, N. Dimov, Z. Ogumi, Carbon-coated Si as a lithium-ion battery anode material, J. Electrochem. Soc. 149 (2002) A1598–A1603.
- [28] H. Li, H. Zhou, Enhancing the performances of Li-ion batteries by carbon-coating: present and future, Chem. Commun. 48 (2012) 1201–1217.
- [29] B.-C. Yu, Y. Hwa, J.-H. Kim, H.-J. Sohn, Carbon coating for Si nanomaterials as high-capacity lithium battery electrodes, Electrochem. Commun. 46 (2014) 144–147.
- [30] N. Dimov, S. Kugino, M. Yoshio, Carbon-coated silicon as anode material for lithium ion batteries: advantages and limitations, Electrochim. Acta 48 (2003) 1579–1587.
- [31] R. Liu, S.M. Mahurin, C. Li, R.R. Unocic, J.C. Idrobo, H. Gao, S.J. Pennycook, S. Dai, Dopamine as a carbon source: the controlled synthesis of hollow carbon spheres and yolk-structured carbon nanocomposites, Angew. Chem. Int. Ed. 123 (2011) 6931–6934.
- [32] J. Kong, W.A. Yee, L. Yang, Y. Wei, S.L. Phua, H.G. Ong, J.M. Ang, X. Li, X. Lu, Highly electrically conductive layered carbon derived from polydopamine and its functions in SnO₂-based lithium ion battery anodes, Chem. Commun. 48 (2012) 10316–10318.
- [33] J. Kong, W.A. Yee, Y. Wei, L. Yang, J.M. Ang, S.L. Phua, S.Y. Wong, R. Zhou, Y. Dong, X. Li, X. Lu, Silicon nanoparticles encapsulated in hollow graphitized carbon nanofibers for lithium ion battery anodes, Nanoscale 5 (2013) 2967–2973.
- [34] S. Fang, L. Shen, Z. Tong, H. Zheng, F. Zhang, X. Zhang, Si nanoparticles encapsulated in elastic hollow carbon fibres for Li-ion battery anodes with high structural stability, Nanoscale 7 (2015) 7409–7414.

- [35] J. Wu, W. Tu, Y. Zhang, B. Guo, S. Li, Y. Zhang, Y. Wang, M. Pan, Poly-dopamine coated graphite oxide/silicon composite as anode of lithium ion batteries, Powder Technol. 311 (2017) 200–205.
- [36] J. Wang, M. Zhou, F. Wu, S. Chen, Electrochemical performance of SiO/C composites as anode material for Li-ion batteries, Adv. Mater. Res. 1092–1093 (2015) 185–190.
- [37] Y. Bie, J. Yang, X. Liu, J. Wang, Y. Nuli, W. Lu, Polydopamine wrapping silicon cross-linked with polyacrylic acid as high-performance anode for lithium-ion batteries, ACS Appl. Mater. Interfaces 8 (2016) 2899–2904.
- [38] M. Gao, D. Wang, X. Zhang, H. Pan, Y. Liu, C. Liang, C. Shang, Z. Guo, A hybrid Si@ FeSi_y/SiO_x anode structure for high performance lithium-ion batteries via ammonia-assisted one-pot synthesis, J. Mater. Chem. 3 (2015) 10767–10776.
- [39] H.K. Han, C. Loka, Y.M. Yang, J.H. Kim, S.W. Moon, J.S. Cho, K.-S. Lee, High capacity retention Si/silicide nanocomposite anode materials fabricated by highenergy mechanical milling for lithium-ion rechargeable batteries, J. Power Sources 281 (2015) 293–300.
- [40] L. Shaw, H. Luo, J. Villegas, D. Miracle, Thermal stability of nanostructured Al₉₃Fe₃Cr₂Ti₂ alloys prepared via mechanical alloying, Acta Mater. 51 (2003) 2647–2663.
- [41] Z. Yang, R. Ren, L.L. Shaw, Evolution of microstructures and nitrogen sorption during high-energy milling of silicon in ammonia, J. Am. Ceram. Soc. 83 (2000) 1807–1004
- [42] R. Ren, Z. Yang, L.L. Shaw, Polymorphic transformation and powder characteristics of TiO₂ during high energy milling, J. Mater. Sci. 35 (2000) 6015–6026.
- [43] H. Sohn, D.H. Kim, R. Yi, D. Tang, S.-E. Lee, Y.S. Jung, D. Wang, Semimicro-size agglomerate structured silicon-carbon composite as an anode material for high performance lithium-ion batteries, J. Power Sources 334 (2016) 128–136.
- [44] C. Liu, Z. Gu, Z. Zhou, Y. Chen, Y. He, X. Xia, H. Liu, Effect of the carbon source on facile synthesized Si/graphite composites and their electrochemical performance, Int. J. Electrochem. Sci. 14 (2019) 5331–5343.
- [45] F. Song, X. Yang, S. Zhang, L.-L. Zhang, Z. Wen, High-performance phosphorus-modified SiO/C anode material for lithium ion batteries, Ceram. Int. 44 (2018) 18509–18515.
- [46] L. Shi, W. Wang, A. Wang, K. Yuan, Z. Jin, Y. Yang, Scalable synthesis of core-shell structured SiOx/nitrogen-doped carbon composite as a high-performance anode material for lithium-ion batteries, J. Power Sources 318 (2016) 184–191.
- [47] S. Fang, Z. Tong, P. Nie, G. Liu, X. Zhang, Raspberry-like nanostructured silicon composite anode for high-performance lithium-ion batteries, ACS Appl. Mater. Interfaces 9 (2017) 18766–18773.
- [48] S.H. Behrens, D.G. Grier, The charge of glass and silica surfaces, J. Chem. Phys. 115 (2001) 6716–6721.
- [49] H. Seidel, L. Csepregi, A. Heuberger, H. Baumgärtel, Anisotropic etching of crystalline silicon in alkaline solutions: I. Orientation dependence and behavior of passivation layers, J. Electrochem. Soc. 137 (1990) 3612–3626.
- [50] H. Seidel, L. Csepregi, A. Heuberger, H. Baumgärtel, Anisotropic etching of crystalline silicon in alkaline solutions: II. Influence of dopants, J. Electrochem. Soc. 137 (1990) 3626–3632.
- [51] I. Zubel, M. Kramkowska, The effect of isopropyl alcohol on etching rate and roughness of (100) Si surface etched in KOH and TMAH solutions, Sens. Actuators, A 93 (2001) 138–147.
- [52] K.P. Rola, I.J.M.T. Zubel, Impact of alcohol additives concentration on etch rate and surface morphology of (100) and (110) Si substrates etched in KOH solutions, Microsyst. Technol. 19 (2013) 635–643.
- [53] X. He, S. Li, W. Ma, Z. Ding, J. Yu, B. Qin, J. Yang, Y. Zou, J. Qiu, A simple and low-cost chemical etching method for controllable fabrication of large-scale kinked silicon nanowires, Mater. Lett. 196 (2017) 269–272.

- [54] C. Zhang, S. Li, W. Ma, Z. Ding, X. Wan, J. Yang, Z. Chen, Y. Zou, J. Qiu, Fabrication of ultra-low antireflection SiNWs arrays from mc-Si using one step MACE, J. Mater. Sci. Mater. Electron. 28 (2017) 8510–8518.
- [55] G. Sheng, Y. Zou, S. Li, W. Ma, Z. Ding, F. Xi, C. Geng, Z. He, Z. Chen, J. Yang, Y. Lei, Controllable nano-texturing of diamond wire sawing polysilicon wafers through low-cost copper catalyzed chemical etching, Mater. Lett. 221 (2018) 85–88.
- [56] A.G. Cullis, L.T. Canham, P.D.J. Calcott, The structural and luminescence properties of porous silicon, J. Appl. Phys. 82 (1997) 909–965.
- [57] O. Bisi, S. Ossicini, L. Pavesi, Porous silicon: a quantum sponge structure for silicon based optoelectronics, Surf. Sci. Rep. 38 (2000) 1–126.
- [58] M.K. Datta, P.N. Kumta, In situ electrochemical synthesis of lithiated silicon-carbon based composites anode materials for lithium ion batteries, J. Power Sources 194 (2009) 1043–1052.
- [59] M.K. Datta, J. Maranchi, S.J. Chung, R. Epur, K. Kadakia, P. Jampani, P.N. Kumta, Amorphous silicon–carbon based nano-scale thin film anode materials for lithium ion batteries, Electrochim. Acta 56 (2011) 4717–4723.
- [60] Y.-M. Kang, S.-M. Lee, S.-J. Kim, G.-J. Jeong, M.-S. Sung, W.-U. Choi, S.-S. Kim, Phase transitions explanatory of the electrochemical degradation mechanism of Si based materials, Electrochem. Commun. 9 (2007) 959–964.
- [61] X. Chen, X. Li, F. Ding, W. Xu, J. Xiao, Y. Cao, P. Meduri, J. Liu, G.L. Graff, J.-G. Zhang, Conductive rigid skeleton supported silicon as high-performance Li-ion battery anodes, Nano Lett. 12 (2012) 4124–4130.
- [62] J. Xie, G. Wang, Y. Huo, S. Zhang, G. Cao, X. Zhao, Nanostructured silicon spheres prepared by a controllable magnesiothermic reduction as anode for lithium ion batteries, Electrochim. Acta 135 (2014) 94–100.
- [63] A. Magasinski, P. Dixon, B. Hertzberg, A. Kvit, J. Ayala, G. Yushin, Highperformance lithium-ion anodes using a hierarchical bottom-up approach, Nat. Mater. 9 (2010) 353–358.
- [64] C. Xu, F. Lindgren, B. Philippe, M. Gorgoi, F. Björefors, K. Edström, T. Gustafsson, Improved performance of the silicon anode for Li-ion batteries: understanding the surface modification mechanism of fluoroethylene carbonate as an effective electrolyte additive, Chem. Mater. 27 (2015) 2591–2599.
- [65] Y. Jin, N.-J.H. Kneusels, L.E. Marbella, E. Castillo-Martínez, P.C.M.M. Magusin, R.S. Weatherup, E. Jónsson, T. Liu, S. Paul, C.P. Grey, Understanding fluoroethylene carbonate and vinylene carbonate based electrolytes for Si anodes in lithium ion batteries with NMR spectroscopy, J. Am. Chem. Soc. 140 (2018) 9854–9867.
- [66] F.J. Günter, J.B. Habedank, D. Schreiner, T. Neuwirth, R. Gilles, G. Reinhart, Introduction to electrochemical impedance spectroscopy as a measurement method for the wetting degree of lithium-ion cells, J. Electrochem. Soc. 165 (2018) A3249–A3256.
- [67] K. Sahni, M. Ashuri, Q. He, R. Sahore, I.D. Bloom, Y. Liu, J.A. Kaduk, L.L. Shaw, H₃PO₄ treatment to enhance the electrochemical properties of Li(Ni_{1/3}Mn_{1/3}Co_{1/3}) O₂ and Li(Ni_{0.5}Mn_{0.3}Co_{0.2})O₂ cathodes, Electrochim. Acta 301 (2019) 8–22.
- [68] T. Umeno, K. Fukuda, H. Wang, N. Dimov, T. Iwao, M. Yoshio, Novel anode material for lithium-ion batteries: carbon-coated silicon prepared by thermal vapor decomposition. Chem. Lett. 30 (2001) 1186–1187.
- [69] K. Fang, M. Wang, Y. Xia, J. Li, Q. Ji, S. Yin, S. Xie, J. Ban, X. Wang, B. Qiu, Facile fabrication of silicon nanoparticle lithium-ion battery anode reinforced with copper nanoparticles, Digest J. Nanomater. Biostructures 12 (2017).
- [70] J. Zhu, C. Gladden, N. Liu, Y. Cui, X. Zhang, Nanoporous silicon networks as anodes for lithium ion batteries, Phys. Chem. Chem. Phys. 15 (2013) 440–443.
- [71] J. Zhu, J. Yang, Z. Xu, J. Wang, Y. Nuli, X. Zhuang, X. Feng, Silicon anodes protected by a nitrogen-doped porous carbon shell for high-performance lithiumion batteries, Nanoscale 9 (2017) 8871–8878.